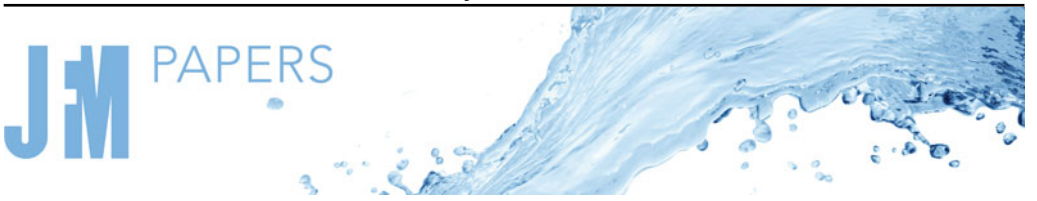
J. Fluid Mech. (2026), *vol.* 1046, A17, doi:10.1017/jfm.2026.12192



How porous medium heterogeneity controls stirring and dispersion

Konstantinos Feroukas[1], **Juan J. Hidalgo**[1], **Daniel Robert Lester**[2] and **Marco Dentz**[1]

[1]Spanish National Research Council (IDAEA-CSIC), Barcelona, Spain

[2]School of Engineering, RMIT University, Melbourne, VIC 3000, Australia

Corresponding author: Marco Dentz, marco.dentz@csic.es

(Received 20 October 2025 UTC; revised 27 April 2026 UTC; accepted 12 September 2026 UTC)

We study stirring and dispersion in steady flow through two-dimensional heterogeneous porous media. A fluid is stirred by the porous medium structure that leads to spatial flow variability and the deformation of fluid elements. While dispersion measures the extension of a solute distribution, stretching underpins solute mixing, chemical reactions and biological activity. Despite this, much less is known about fluid stretching in porous media. Its relation to the dispersion process on the one hand and the flow and medium properties on the other remain open questions. To close this gap, we probe the heterogeneity mechanisms that are at the origin of stretching and dispersion of fluid elements, and quantify the upscaled laws that govern their dynamics. Thus we perform detailed numerical simulations of Darcy flow in two-dimensional porous media characterised by a spatially varying hydraulic conductivity. Dispersion is analysed in terms of first-passage time distributions of fluid elements and the temporal evolution of their displacement mean and variance, while deformation is studied in terms of the probability density function and average elongation of fluid elements. We find that the dispersion and stretching behaviours are closely related. The exponents that govern the decay of the first-passage time distributions and evolution of the displacement variances also determine the evolution of the mean elongation. This dynamics is quantified in a single upscaled theoretical framework that bridges between Eulerian flow structure, large-scale dispersion and stretching of fluid elements.

Key words: porous media, dispersion, laminar mixing

© The Author(s), 2026. Published by Cambridge University Press. This is an Open Access article, distributed under the terms of the Creative Commons Attribution-NonCommercial licence (https://creativecommons.org/licenses/by-nc/4.0/), which permits non-commercial re-use, distribution, and reproduction in any medium, provided the original article is properly cited. The written permission of Cambridge University Press or the rights holder(s) must be obtained prior to any commercial use.

https://doi.org/10.1017/jfm.2026.12192 Published online by Cambridge University Press

1. Introduction

Flow and solute transport in heterogeneous porous and fractured media is determined by the spatial variability of hydraulic conductivity, which may vary over orders of magnitude (Bear 1972). Steady flows through such media are characterised by organisation of the flow along the characteristic length scales of the medium, and broad distributions of flow speeds and thus residence times of transported scalars. These features affect both the transport and deformation of fluid elements, and the mixing and dispersion of passive and reactive scalars. They lead to non-Fickian large-scale transport properties, which manifest in broad distributions of first-passage times and nonlinear evolutions of dispersion.

Although closely related, dispersion, stirring and mixing are distinct physical processes that control solute transport and dilution (Villermaux 2019). In porous or fractured media, the medium itself stirs the fluid as it permeates through the medium driven by a pressure gradient. At the pore scale, the medium stirs the fluid by the flow variability in the complex pore space (Lester *et al.* 2013), which has been investigated experimentally (Souzy *et al.* 2020; Heyman *et al.* 2020) and numerically (Lester *et al.* 2016). In the three-dimensional pore space, advection is typically chaotic (Lester *et al.* 2025) and stretching exponential. This is different on the Darcy scale. First, for steady flow in isotropic porous media, advection cannot be chaotic due to topological constraints (Lester *et al.* 2022), that is, stretching is necessarily sub-exponential. Second, the medium stirs the bulk fluid through spatial variations in permeability, which causes flow variability and generates local velocity gradients. This leads to the deformation of fluid or solute fronts, which increases concentration gradients, promotes diffusive mass transfer and thus solute mixing, chemical reactions and biological processes.

Here, we address the question of how variations in the Darcy-scale medium heterogeneity act on the dispersion and stretching of fluid elements. Although dispersion and stretching are closely related in steady porous medium flows, there also are important differences. Longitudinal dispersion is solely governed by velocity fluctuations along streamlines (Gelhar 1993; Berkowitz *et al.* 2006; Dagan 2012), whereas transverse dispersion is controlled by the geometry of the streamlines (Lester *et al.* 2023). Conversely, fluid stirring is controlled by velocity gradients (shear and vorticity) normal to streamlines (Dentz *et al.* 2016*b*). Although they are distinct, these processes are governed by the underlying hydraulic conductivity field, hence strong links may be expected between them. It is important to point out that the dispersion of fluid elements and solute particles are equal in the limit of purely advective transport. Solute dispersion is in general dependent on the Péclet number, which measures the ratio between the characteristic diffusion and advection time scales. Here, we focus on the dispersion and stretching of fluid elements. The two processes are illustrated in figure 1 that shows both the dispersion and deformation of a material line.

Stochastic modelling (Rubin 2003) provides a framework to systematically quantify the spatial variability of hydraulic conductivity and its impact on flow and transport. In this framework, hydraulic conductivity is typically modelled as a multi-Gaussian spatial random field with log-normal distribution of conductivity point values (Gelhar 1993; Dagan 2012). Although criticised for the lack of connectivity of high permeability zones (Gómez-Hernández & Wen 1998) and the assumption of Gaussianity of the log increments (Painter 1996), the multi-Gaussian representation is as an idealised model both simple enough to lead to general conclusions and complex enough to disclose some sufficient conditions between medium heterogeneity and dispersion. Perturbation theory (Gelhar & Axness 1983) predicts the asymptotic value of longitudinal dispersion as a

https://doi.org/10.1017/jfm.2026.12192 Published online by Cambridge University Press

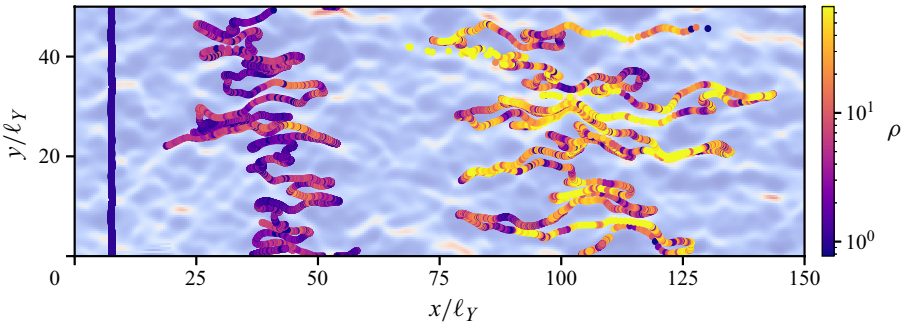


Figure 1. Evolution of particles initially positioned perpendicularly to the mean flow. The particle positions are shown for $t = 0$, $t = 50\tau_v$ and $t = 100\tau_v$, where $\tau_v = \ell_Y/\langle u \rangle$ with ℓ_Y the characteristic heterogeneity length scale. The colouring of the particles is proportional to the accumulated stretching experienced by each particle, defined as ρ. The background shows the longitudinal velocity as a colormap from blue to red (low to high velocity zones). The variance of the log of permeability used for this figure is $\sigma_f^2 = 1$ and the number of particles $N_p = 10^4$. The figure illustrates a solute occupying space from left to right separated by the propagation front. The high deformed zones of the front will be where the solute will be more prompt to mixing and thus to reactions between the invading and invaded fluids.

function of heterogeneity through the variance of the log conductivity, the characteristic correlation scale and the mean velocity. For increasing variance, however, the linear relation between the dispersion coefficient and log-conductivity variance breaks down (Fiori *et al.* 2003; de Dreuzy *et al.* 2007; Gotovac *et al.* 2009). Furthermore, the asymptotic regime may be reached only at extremely large times, and transport can in general not be described in terms of the advection–dispersion equation characterised by the average flow velocity and constant macrodispersion coefficients (Adams & Gelhar 1992; Levy & Berkowitz 2003; Kang *et al.* 2015). Approaches to account for non-Fickian or anomalous large-scale dispersion include spatio-temporally non-local advection–dispersion equations (Neuman & Tartakovsky 2009), fractional advection–dispersion equations and multi-rate mass transfer approaches (Frippiat & Holeyman 2008), continuous time random walk (CTRW) (Berkowitz *et al.* 2006) and time domain random walk models (Noetinger *et al.* 2016). In this work we employ the CTRW as an upscaling approach that acknowledges the spatial correlation of particle speeds and the impact of broad residence time distributions on the large-scale particle dynamics (Berkowitz *et al.* 2006; Le Borgne *et al.* 2008; Dentz *et al.* 2016*a*; Comolli *et al.* 2019).

The deformation of elementary fluid volumes by velocity gradients is a key process for scalar mixing, chemical reactions and biological processes in fluid flows. Stretching rates are a key input into mixing theories, along with the Péclet number, that compares diffusive and advective mass transfer over a characteristic length scale (Villermaux 2019). Fluid deformation has been the subject of research over decades in unsteady turbulent flows (Cocke 1969; Ashurst *et al.* 1987; Villermaux 2019). Flows through porous and fractured media, albeit often steady, can be analysed in a similar way due to the complexity induced by the medium structure. One important difference is that the steady nature of the flow imposes topological constraints in that pathlines of the flow are invariant, forming fixed streamlines that govern stirring and dispersion. One consequence of this constraint is that one of the principal directions of the deformation gradient tensor must coincide with the local velocity direction (Tabor 1992). Additionally, the magnitude of this principal deformation is directly proportional to the local velocity magnitude, prohibiting net stretching along the flow direction and only allowing persistent stretching and contraction in the directions normal to the flow (Lester *et al.* 2018). Furthermore, for divergence-free

https://doi.org/10.1017/jfm.2026.12192 Published online by Cambridge University Press

flow, the sum of the principal stretching rates (often characterised as Lyapunov exponents) must be zero. Hence, steady three-dimensional flow can only exhibit one unique Lyapunov exponent.

In this study we focus attention on stretching and dispersion in steady two-dimensional (2-D) flows in heterogeneous porous media. For steady 2-D flows, this stretching dynamics is even further constrained by the reduction in the geometric degrees of freedom. From the arguments above, the Lyapunov exponent in these flows must be zero (Metcalfe *et al.* 2023), corresponding to sub-exponential (non-chaotic) fluid stretching. These topological constraints also limit transverse dispersion to be zero in the purely advective limit (Attinger *et al.* 2004), as invariant streamlines are confined to 2-D surfaces, hence neighbouring streamlines cannot continually separate as they are advected. Although these constraints appear to strongly limit the applicability of studies of flow and transport in 2-D porous media, they actually are directly relevant to steady 3-D flow in an important class of heterogeneous porous materials with isotropic hydraulic conductivity fields. For steady 3-D flow in this class of porous materials, the helicity density $\mathcal{H}(\boldsymbol{x}) \equiv \boldsymbol{u}(\boldsymbol{x}) \cdot (\boldsymbol{\nabla} \times \boldsymbol{u}(\boldsymbol{x}))$, where $\boldsymbol{u}(\boldsymbol{x})$ is the Eulerian flow velocity (Moffatt 1969) is identically zero (Sposito 1994), meaning that they are non-chaotic and their streamlines are confined to families of 2-D streamsurfaces (Lester *et al.* 2021) within the flow. As such, the dynamics of fluid dispersion (Lester *et al.* 2023) and stretching Lester *et al.* (2022) in steady 3-D flow in isotropic heterogeneous porous media is very similar to that of steady 2-D flow in heterogeneous porous media.

Coupled CTRW models have been proposed (Dentz *et al.* 2016*b*; Lester *et al.* 2018) to analyse deformation in 2-D and 3-D steady random flows. While these studies show that algebraic (sub-exponential) stretching in 2-D steady random flows is driven by correlations between velocity and shear, the link between these stretching rates and medium properties for heterogeneous Darcy flow is not established. Le Borgne *et al.* (2015) study stretching in 2-D porous media, and propose a multiplicative stochastic process to describe stretching evolution, which, however, needs to be calibrated by observations of the stretching process itself and does not reveal its relation to the flow field of medium structure, nor its relation to the dispersion dynamics.

In this paper, we aim to close these gaps by simultaneously analysing the dispersion and deformation of fluid elements in 2-D heterogeneous porous media. The analysis of particle velocities and deformation along streamlines will provide insights into the heterogeneity-induced stochastic dynamics of these processes, and identify the relevant heterogeneity mechanisms. This allows us to link the large-scale stretching and dispersion behaviours to the underlying Eulerian flow organisation and medium structure. Beyond the fundamental interest of flow and deformation in 2-D porous media, they are relevant for example, in the context of aquifers whose extension is much larger than their depth, for flow and advection-dominated transport in rough fractures and in 3-D isotropic porous media.

The paper is organised as follows. Section 2 presents the governing equations for flow, particle transport and fluid deformation and the numerical methodology. Section 3 develops the stochastic model for fluid deformation and dispersion, and § 4 discusses how the medium heterogeneity controls the dispersion and deformation behaviours observed in heterogeneous porous media in the light of this model. Section 5 provides a summary and conclusions.

2. Methodology

We introduce here the continuum-scale flow model for porous media, the kinematic equations for particle motion and fluid deformation and the observables of interest.

https://doi.org/10.1017/jfm.2026.12192 Published online by Cambridge University Press

2.1. *Flow*

We consider flow through a 2-D continuum-scale heterogeneous porous medium, which is described by the Darcy equation (Bear 1972)

$$\boldsymbol{q}(\boldsymbol{x}) = -K(\boldsymbol{x})\nabla h(\boldsymbol{x}), \tag{2.1}$$

where $\boldsymbol{x} = (x_1, x_2)^\top$ is the position vector, $\boldsymbol{q}$ denotes the Darcy velocity, $K(\boldsymbol{x})$ hydraulic conductivity and $h(\boldsymbol{x})$ hydraulic head. Both the fluid and the solid matrix are considered incompressible such that $\nabla \cdot \boldsymbol{q} = 0$, which yields the groundwater flow equation

$$K(\boldsymbol{x})\nabla^2 h(\boldsymbol{x}) + \nabla K(\boldsymbol{x}) \cdot \nabla h(\boldsymbol{x}) = 0. \tag{2.2}$$

The spatially variable hydraulic conductivity field $K(\boldsymbol{x})$ is modelled as a multi-Gaussian random field (Rubin 2003). Its marginal probability density function (PDF), that is the distribution of the point values of $K(\boldsymbol{x})$, is denoted by $p_K(k)$. In this work, we consider the log-normal and gamma distributions

$$p_K(k) = \frac{\exp\left[-\dfrac{(\ln k - \mu_f)^2}{2\sigma_f^2}\right]}{k\sqrt{2\pi\sigma_f^2}}, \qquad p_K(k) = \left(\frac{k}{k_0}\right)^{\alpha-1} \frac{\exp(-k/k_0)}{\Gamma(\alpha)k_0}, \tag{2.3}$$

respectively, where $\Gamma(\alpha)$ denotes the gamma function. The log-normal PDF is characterised by the mean μ_f and variance σ_f^2 of $f(\boldsymbol{x}) = \ln K(\boldsymbol{x})$ and the gamma distribution by the exponent α and the scale k_0.

The conductivity fields $K(\boldsymbol{x})$ are derived from the stationary multivariate Gaussian random fields $Y(\boldsymbol{x})$, which are characterised by a unit Gaussian marginal density, that is, they have zero mean and unit variance $\sigma_Y^2 = \langle Y(\boldsymbol{x})^2 \rangle = 1$. The angular brackets denote the ensemble average over all realisations of $Y(\boldsymbol{x})$. The covariance function of $Y(\boldsymbol{x})$ is denoted by

$$\langle Y(\boldsymbol{x})Y(\boldsymbol{x}')\rangle = C_Y(\boldsymbol{x} - \boldsymbol{x}'). \tag{2.4}$$

In this work, we employ the isotropic Gaussian covariance function

$$C_Y(\boldsymbol{x}) = \exp\left(-\frac{\boldsymbol{x}^2}{2\ell_Y^2}\right), \tag{2.5}$$

where ℓ_Y denotes the correlation length. The conductivity field is obtained according to the point-wise transform

$$K(\boldsymbol{x}) = P_K^{-1}(\Phi[Y(\boldsymbol{x})]), \tag{2.6}$$

where $P_K(k)$ is the cumulative distribution function (CDF) of $p_K(k)$, $P_K^{-1}(u)$ its inverse and $\Phi(y)$ is the CDF of the unit Gaussian PDF. For the log-normal distribution, the map is given by

$$K(\boldsymbol{x}) = \exp[f(\boldsymbol{x})], \qquad f(\boldsymbol{x}) = \mu_f + \sigma_f Y(\boldsymbol{x}). \tag{2.7}$$

For the gamma distribution, there is no analytical expression for the map between $Y(\boldsymbol{x})$ and $K(\boldsymbol{x})$ and we use the inverse or Smirnov transform method (Devroye 1986). Note that the effective hydraulic conductivity for log-normally distributed $K(\boldsymbol{x})$ is equal to the geometric mean conductivity $\exp(\mu_f)$ (Keller 1964; Rubin 2003). In the following we set $\mu_f = 0$, which is equivalent to normalising all the log-normal $K(\boldsymbol{x})$ fields by their effective conductivity.

https://doi.org/10.1017/jfm.2026.12192 Published online by Cambridge University Press

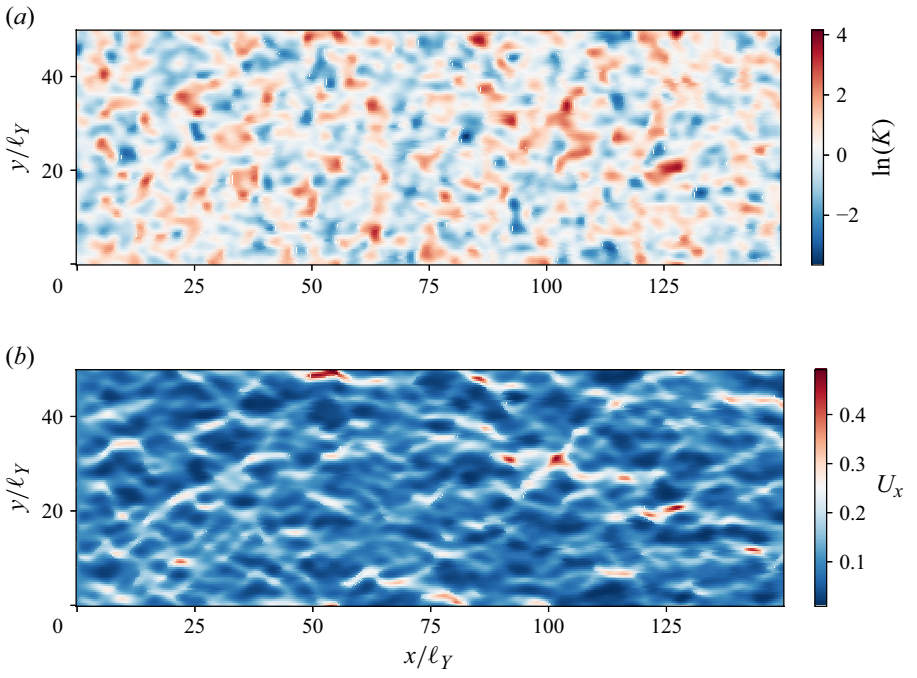


Figure 2. (*a*) Log-normal hydraulic conductivity field with $\sigma_f^2 = 1$. (*b*) Distribution of streamwise velocities for the corresponding log-normally distributed hydraulic conductivity field.

We consider constant head boundary conditions such that the mean Darcy velocity $\langle \boldsymbol{q}(\boldsymbol{x}) \rangle$ is constant and aligned with the x_1-direction of the coordinate system. The flow velocity is denoted by $\boldsymbol{u}(\boldsymbol{x}) = \boldsymbol{q}(\boldsymbol{x})/\phi$, where ϕ is porosity. Porosity is here assumed to be constant and set to one, which is equivalent to rescaling time. We refer in the following to $\boldsymbol{u}(\boldsymbol{x})$ as the Eulerian velocity and to its magnitude $u(\boldsymbol{x}) \equiv |\boldsymbol{u}(\boldsymbol{x})|$ as the Eulerian speed. The PDF of $u(\boldsymbol{x})$ is denoted by $p_e(u)$. It is obtained by spatial sampling according to

$$p_e(u) = \lim_{V \to \infty} \frac{1}{V} \int_{\Omega} \mathrm{d}\boldsymbol{x}\, \delta[u - u(\boldsymbol{x})|], \tag{2.8}$$

with Ω is the sampling domain, V its volume. Due to ergodicity, spatial sampling of $u(x)$ is equivalent to ensemble sampling, and thus, $p_e(u) = \langle \delta[u - u(\boldsymbol{x})] \rangle$. The ratio between the mean flow speed and the mean streamwise flow velocity defines the advective tortuosity χ (Comolli *et al.* 2019)

$$\chi = \frac{\langle u(\boldsymbol{x}) \rangle}{\langle u_1(\boldsymbol{x}) \rangle}. \tag{2.9}$$

The numerical methodology for the generation of the hydraulic conductivity fields and the numerical solution for the Darcy flow field $\boldsymbol{q}(\boldsymbol{x})$ are detailed in Appendix B. Figure 2 illustrates a multi-Gaussian spatial random field and the distribution of streamwise velocities for a log-normal hydraulic conductivity distribution. For the numerical simulations used in §§ 3 and 4 we consider a log-normally distributed $K(\boldsymbol{x})$ characterised by $\sigma_f^2 = 0.25, 1, 3, 6$, and a gamma-distributed $K(\boldsymbol{x})$ with $\alpha = 0.25, 0.5, 0.75$.

https://doi.org/10.1017/jfm.2026.12192 Published online by Cambridge University Press

2.2. *Particle motion*

The position $\boldsymbol{x}(t, \boldsymbol{a})$ of a particle originating at $\boldsymbol{x}(t=0, \boldsymbol{a}) = \boldsymbol{a}$ is described by the kinematic equation

$$\frac{\mathrm{d}\boldsymbol{x}(t, \boldsymbol{a})}{\mathrm{d}t} = \boldsymbol{v}(t, \boldsymbol{a}), \tag{2.10}$$

where $\boldsymbol{v}(t, \boldsymbol{a}) \equiv \boldsymbol{u}[\boldsymbol{x}(t, \boldsymbol{a})]$ is the isochronically sampled Lagrangian velocity. The distance $s(t, \boldsymbol{a})$ a particle travels along a streamline satisfies

$$\frac{\mathrm{d}s(t, \boldsymbol{a})}{\mathrm{d}t} = v(t, \boldsymbol{a}), \tag{2.11}$$

where $v(t, \boldsymbol{a}) \equiv |\boldsymbol{v}(t, \boldsymbol{a})|$ is the isochronically sampled Lagrangian speed. Its PDF is denoted by $p_t(v)$. It is equal to the PDF of Eulerian flow speeds, $p_t(v) = p_e(v)$ (Dentz *et al.* 2016*a*; Comolli *et al.* 2019).

We can express the advection equation (2.10) as a function of distance s along the streamline by using the map (2.11) from $t \to s$, which gives

$$\frac{\mathrm{d}\boldsymbol{x}(s, \boldsymbol{a})}{\mathrm{d}s} = \frac{\boldsymbol{v}(s, \boldsymbol{a})}{v(s, \boldsymbol{a})}, \qquad \frac{\mathrm{d}t}{\mathrm{d}s} = \frac{1}{v(s, \boldsymbol{a})}, \tag{2.12}$$

where $\boldsymbol{v}(s) \equiv \boldsymbol{u}[\boldsymbol{x}(s, \boldsymbol{a})]$ is the equidistant Lagrangian velocity. Its magnitude defines the equidistance Lagrangian speed $v(s, \boldsymbol{a}) \equiv |\boldsymbol{v}(s, \boldsymbol{a})|$. Its PDF is denoted by $p_s(v)$. It is related to the Eulerian speed PDF $p_e(v)$ by flux weighting (Dentz *et al.* 2016*a*; Comolli *et al.* 2019)

$$p_s(v) = \frac{v p_e(v)}{\langle u \rangle}. \tag{2.13}$$

The initial particle positions are distributed along a line of length $L \gg \ell_Y$ perpendicular to the mean flow, either uniformly or flux weighted. The initial particle distribution is denoted by $\rho(\boldsymbol{a})$. For a uniform initial distribution, $\rho(\boldsymbol{a}) = L^{-1}\delta(a_1)$, where a_1 is the first coordinate of the vector $\boldsymbol{a}$. This initial distribution corresponds to the initial speed distribution $p_0(v) = p_e(v)$. The numerical particle tracking methodology is detailed in Appendix B.

2.3. *Fluid deformation*

We focus on the evolution of the elongation of an infinitesimal material fluid element, whose length and orientation are described by the vector $\boldsymbol{z}(t, \boldsymbol{a}) = \boldsymbol{x}(t, \boldsymbol{a} + \delta\boldsymbol{a}) - \boldsymbol{x}(t, \boldsymbol{a})$. For simplicity of notation, in the following we set $\boldsymbol{z}(t) = \boldsymbol{z}(t, \boldsymbol{a})$ and drop the argument $\boldsymbol{a}$ indicating the initial position throughout. The evolution of $\boldsymbol{z}(t)$ is governed by

$$\frac{\mathrm{d}\boldsymbol{z}(t)}{\mathrm{d}t} = \boldsymbol{\epsilon}(t)\boldsymbol{z}(t), \tag{2.14}$$

where the velocity gradient is defined by $\boldsymbol{\epsilon}(t) = \boldsymbol{\nabla} \otimes \boldsymbol{u}[\boldsymbol{x}(t, \boldsymbol{a})]^\top \equiv \boldsymbol{\nabla}\boldsymbol{v}(t)^\top$. The transpose is denoted by $\top$. The initial condition is given by $\boldsymbol{z}(t=0) = \delta\boldsymbol{a}$.

Note that the evolution of the infinitesimal line element $\boldsymbol{z}(t)$ is also related to the deformation gradient tensor $\boldsymbol{F}(t) \equiv \mathrm{d}\boldsymbol{x}/\mathrm{d}\boldsymbol{a}$ that characterises the transform between the Eulerian and and Lagrangian frames as $\boldsymbol{z}(t) = \boldsymbol{F}(t)\boldsymbol{z}(0)$, and analogous to (2.14), $\boldsymbol{F}(t)$ evolves as $\dot{\boldsymbol{F}}(t) = \boldsymbol{\epsilon}(t)\boldsymbol{F}(t)$. The Cauchy–Green tensor $\boldsymbol{C}(t) = \boldsymbol{F}(t)^\top \boldsymbol{F}(t)$ which characterises fluid deformation plays a central role in controlling e.g. solute mixing and chemical reactions, hence stretching of the line element $\boldsymbol{z}(t)$ is intimately related to these fluid-borne processes.

https://doi.org/10.1017/jfm.2026.12192 Published online by Cambridge University Press

Equation (2.14) is transformed into the coordinate system aligned with the streamline along which the fluid particle is moving (Dentz *et al.* 2016*b*). The transformation is performed through the rotation matrix defined by

$$\boldsymbol{A}(t) = \frac{1}{v(t)} \begin{bmatrix} v_1(t) & -v_2(t) \\ v_2(t) & v_1(t) \end{bmatrix}. \tag{2.15}$$

We refer to these coordinates as Protean coordinates in the following (Adachi 1983). The strip $\boldsymbol{z}(t)$ is transformed according to

$$\boldsymbol{z}'(t) = \boldsymbol{A}^\top(t)\boldsymbol{z}(t). \tag{2.16}$$

Thus, we obtain for the evolution of $\boldsymbol{z}'(t)$

$$\frac{\mathrm{d}\boldsymbol{z}'(t)}{\mathrm{d}t} = \boldsymbol{\epsilon}'(t)\boldsymbol{z}'(t), \tag{2.17}$$

where the velocity gradient transforms as a pseudotensor

$$\boldsymbol{\epsilon}'(t) = \boldsymbol{A}^\top(t)\boldsymbol{\epsilon}(t)\boldsymbol{A}(t) + \frac{\mathrm{d}\boldsymbol{A}^\top(t)}{\mathrm{d}t}\boldsymbol{A}(t); \tag{2.18}$$

see also Appendix A. In the following, we drop the primes for simplicity of notation. The transformed velocity gradient tensor has the upper triangular form

$$\boldsymbol{\epsilon}(t) = \begin{bmatrix} \epsilon_{11}(t) & \sigma(t) \\ 0 & -\epsilon_{11}(t) \end{bmatrix}. \tag{2.19}$$

Its components are given by

$$\epsilon_{11}(t) = \frac{1}{v(t)}\frac{\mathrm{d}v(t)}{\mathrm{d}t}, \tag{2.20}$$

$$\sigma(t) = \frac{1}{v(t)^2}\left[v_1(t)^2\sigma(t) - v_2(t)^2\sigma(t) - 4v_1(t)v_2(t)\epsilon_{11}(t)\right]. \tag{2.21}$$

We defined the shear rate as $\sigma(t) = \epsilon_{12}(t) + \epsilon_{21}(t)$. Due to incompressibility, $\epsilon_{22}(t) = -\epsilon_{11}(t)$. Using the upper triangular form of $\boldsymbol{\epsilon}(t)$, the kinematic equation (2.17) can be integrated explicitly, which gives

$$z_1(t) = \frac{v(t)}{v(0)}\left[z_1(0) + z_2(0)\int_0^t \mathrm{d}t\sigma(t)\frac{v(0)^2}{v(t)^2}\right], \tag{2.22a}$$

$$z_2(t) = \frac{v(0)}{v(t)}z_2(0). \tag{2.22b}$$

These equations show that the principal stretches given by the diagonal components $\epsilon'_{11}(t)$ of $\boldsymbol{\epsilon}(t)$ generate zero net stretching as they directly generate the fluctuating terms $v(t)/v(0)$ and $v(0)/v(t)$ in (2.22*a*), (2.22*b*), respectively. Hence, not only are the Lyapunov exponents associated with these principal stretching directions zero, but the time-averaged principal stretches are likewise. Conversely, the off-diagonal component $\sigma'(t)$ of $\boldsymbol{\epsilon}(t)$ (which corresponds to a fluctuating shear) leads to persistent algebraic stretching of fluid elements, as reflected by the integral in (2.22*a*). Note that rotation into the streamline coordinate system (2.15) corresponds to enforcement of the topological constraints (discussed in § 1) associated with the existence of streamlines in steady flow. Here, the alignment of the coordinate frame with the streamlines recovers the zero Lyapunov exponent inherent to steady 2-D flow, whereas naive stochastic models of fluid

https://doi.org/10.1017/jfm.2026.12192 Published online by Cambridge University Press

stretching based on (2.14) require *ad hoc* approaches to enforce sub-exponential line growth (Le Borgne *et al.* 2013, 2015). This example reinforces how flow topology controls mixing and transport in porous media.

Equations (2.22*a*), (2.22*b*) can be formulated in terms of equidistant sampling through the variable change $t \to s$. That is, we set $\mathrm{d}t = ds/v(s)$ in (2.22) to obtain

$$z_1(s) = \frac{v(s)}{v(0)} z_1(0) + v(s)v(0)z_2(0)\zeta(s), \qquad \zeta(s) = \int_0^s \mathrm{d}s \frac{\sigma(s)}{v(s)^3}, \tag{2.23a}$$

$$z_2(s) = \frac{v(0)}{v(s)} z_2(0). \tag{2.23b}$$

The strip vector at time t is then given by

$$\boldsymbol{z}(t) = \boldsymbol{z}[s(t)]. \tag{2.24}$$

The strip length is given by $\ell(t) = |\boldsymbol{z}(t)| = \sqrt{z_1(t^2) + z_2(t)^2}$, its initial length by $\ell(t=0) = \ell_0 = |\delta \boldsymbol{a}|$. The numerical methodology for the solution of the deformation problem is detailed in Appendix B.

2.4. *Observables*

Figure 3 illustrates the evolution of the dispersion of a line source of fluid particles and the length and orientation of fluid elements in a heterogeneous Darcy velocity field. In the following, we define the observables to probe the dispersion and deformation behaviours. The evaluation of the observables from the detailed numerical transport and deformation simulations is detailed in Appendix B.

2.4.1. *Dispersion*

We consider the displacement mean and variance of longitudinal particle position average across different realisations of the hydraulic conductivity field

$$\mu(t) = \left\langle \int \mathrm{d}\boldsymbol{a}\, \rho(\boldsymbol{a}) x_1(t, \boldsymbol{a}) \right\rangle, \qquad \kappa(t) = \left\langle \int \mathrm{d}\boldsymbol{a}\, \rho(\boldsymbol{a})\, [x_1(t, \boldsymbol{a}) - \mu(t)]^2 \right\rangle. \tag{2.25}$$

The displacement mean indicates the average longitudinal position of the tortuous line shown in figure 3, and the displacement variance its dispersion.

The residence or transit times of fluid particles between the inlet and a control position are measured by the first-passage time defined by

$$\tau(x_1, \boldsymbol{a}) = \min\left[t \mid x_1(t, \boldsymbol{a}) \geqslant x_1\right]. \tag{2.26}$$

The distribution of first-passage times $f(t, x_1)$ or breakthrough curves is obtained by sampling over all particles for a given realisation and averaging over all disorder realisations

$$f(t, x_1) = \left\langle \int \mathrm{d}\boldsymbol{a}\, \rho(\boldsymbol{a})\, \delta[t - t(x_1 \chi)] \right\rangle. \tag{2.27}$$

2.4.2. *Lagrangian deformation*

We consider the mean elongation of a material strip as a measure for the average fluid deformation

$$\lambda(t) = \langle \ell(t) \rangle. \tag{2.28}$$

https://doi.org/10.1017/jfm.2026.12192 Published online by Cambridge University Press

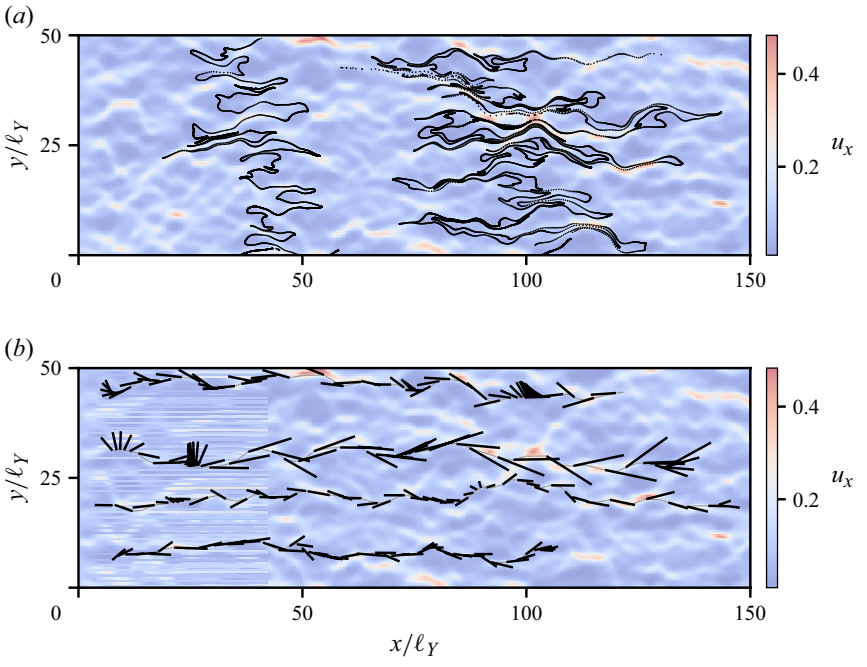


Figure 3. (*a*) Evolution of a set of 10^5 particles that are initially distributed uniformly along a line perpendicular to the mean flow direction in a log-normal conductivity field with $\sigma_f^2 = 1$ and $\ell_Y = 1$. Particle positions are shown at $t = 20\tau_v$ and $t = 90\tau_v$ illustrating longitudinal dispersion. (*b*) Illustration of line stretching and rotation in the same flow field as in the (*a*). The black solid lines show the evolution of the vector $\boldsymbol{z}(t, \boldsymbol{a})$ for four different initial positions $\boldsymbol{a}$, obtained by numerical integration of (2.14) along the trajectories $\boldsymbol{x}(t, \boldsymbol{a})$ shown by the light grey solid lines, which are obtained by numerical integration of (2.10) as described in Appendix B. The background is a map of the flow magnitude.

Furthermore, we consider the PDF of $\ell(t)$, which is obtained through averaging over all particles in single realisations and over the ensemble of disorder realisations, as

$$p_\ell(l) = \left\langle \int \mathrm{d}\boldsymbol{a}\, \rho(\boldsymbol{a})\, \delta[l - \ell(t, \boldsymbol{a})] \right\rangle. \tag{2.29}$$

3. Stochastic dynamics of stretching

Based on the formulation of stretching in the Protean frame outlined in § 2.3, here, we derive a CTRW approach for fluid deformation in heterogeneous porous media that provides both a link to the dispersion process and to the flow and medium structure. We first recall the CTRW formulation for particle dispersion in § 3.1. Then we develop the model for fluid deformation based on the analysis of the statistical properties of shear rate series in § 3.2. The two stochastic models are synthesised in a single CTRW approach for stretching and dispersion in § 3.3.

3.1. *Continuous time random walk for particle dispersion*

The kinematic equations (2.12) for streamwise particle motion are written as (Comolli *et al.* 2019; Dentz & Hyman 2023; Dentz & Massoudieh 2025)

https://doi.org/10.1017/jfm.2026.12192 Published online by Cambridge University Press

$$\frac{\mathrm{d}x_1(s)}{ds} = \chi^{-1}, \qquad \frac{\mathrm{d}t(s)}{ds} = \frac{1}{v(s)}, \tag{3.1}$$

where the streamline distance is projected onto the streamwise distance by tortuosity χ. Following Le Borgne *et al.* (2008) and Dentz *et al.* (2016*a*), the speed series $\{v(s)\}$ is modelled as a stationary Markov process. Note that, here, the particle trajectories depend on the initial condition only through the initial velocity distribution. The explicit dependence on $\boldsymbol{a}$ is dropped due to the ergodicity of the stochastic process that models particle motion.

The stationary distribution of $\{v(s)\}$ is given by $p_s(v)$, which is defined in terms of the Eulerian speed distribution by (2.13). The initial distribution of particle positions $\rho(\boldsymbol{a})$ translates in this framework into a distribution of initial velocities $p_0(v)$, which correspond to the velocities that the particle sampled in the injection zone. The Markov process for particle speeds is defined in terms of the normal score transform of $v(s)$

$$w(s) = \Phi^{-1}\{P_s[v(s)]\}, \qquad v(s) = P_s^{-1}(\phi[w(s)]), \tag{3.2}$$

where $\Phi(w)$ is the cumulative density function (CDF) of the unit Gaussian PDF $\phi(w)$, and $P_s(v)$ is the CDF of the stationary speed PDF $p_s(v)$. The series $\{w(s)\}$ of normal scores is by definition Gaussian distributed. The evolution of $w(s)$ is modelled by the Ornstein–Uhlenbeck process (Morales *et al.* 2017; Hakoun *et al.* 2019)

$$\frac{\mathrm{d}w(s)}{\mathrm{d}s} = -w(s)\ell_c^{-1} + \sqrt{2\ell_c^{-1}}\eta_1(s), \tag{3.3}$$

which implies that it is also stationary (Doob 1942). The random function $\eta_1(s)$ denotes a unit Gaussian white noise. In the following, we use the notation $\eta_i(s)$ $(i = 1, 2, \ldots)$ to refer to independent unit Gaussian random noises. The two $\eta_i(s)$ and $\eta_k(s)$ are independent for $i \neq k$.

This formulation is equivalent to generating the speed series by a Gaussian copula (Dentz & Hyman 2023; Dentz & Massoudieh 2025). The CTRW (3.1) based on the speed process described above represents a stochastic model for particle motion in steady random flows and has been used for the modelling of dispersion from the pore to the reservoir scales in porous and fractured media (Puyguiraud *et al.* 2019; Comolli *et al.* 2019; Hyman & Dentz 2021).

In this framework, the displacement mean and variance in streamwise direction are

$$\mu(t) = \chi^{-1}\langle s(t)\rangle, \qquad \kappa(t) = \chi^{-2}\langle[s(t) - \langle s(t)\rangle]^2\rangle, \tag{3.4}$$

where $s(t) = \max[s|t(s) \leqslant t]$. The angular brackets here denote the ensemble average over all particle realisations. The first-passage time distribution is

$$f(t, x_1) = \langle\delta[t - t(x_1\chi)]\rangle, \tag{3.5}$$

where $t(s)$ is given by (3.1).

3.2. *Stochastic dynamics of deformation*

The deformation process, given by (2.23) depends on the speed series $\{v(s)\}$ and the series of shear rates $\{\sigma(s)\}$. In fact, the auxiliary process $\zeta(s)$ defined in (2.23*a*) evolves as

$$\frac{\mathrm{d}\zeta(s)}{\mathrm{d}s} = \frac{\sigma(s)}{v(s)^3}. \tag{3.6}$$

The upscaled model for Lagrangian fluid deformation requires definition of the stochastic process for the series of shear rates $\{\sigma(s)\}$, which is correlated with the particle

https://doi.org/10.1017/jfm.2026.12192 Published online by Cambridge University Press

	$\sigma_f^2 = 0.25$	$\sigma_f^2 = 1$	$\sigma_f^2 = 3$
k_c	0.029	0.065	0.097
	$\alpha = 0.75$	$\alpha = 0.5$	$\alpha = 0.25$
k_c	0.074	0.074	0.074

Table 1. Values of k_c, see (3.7), for the (bottom) gamma-distributed and (top) log-normal conductivity fields.

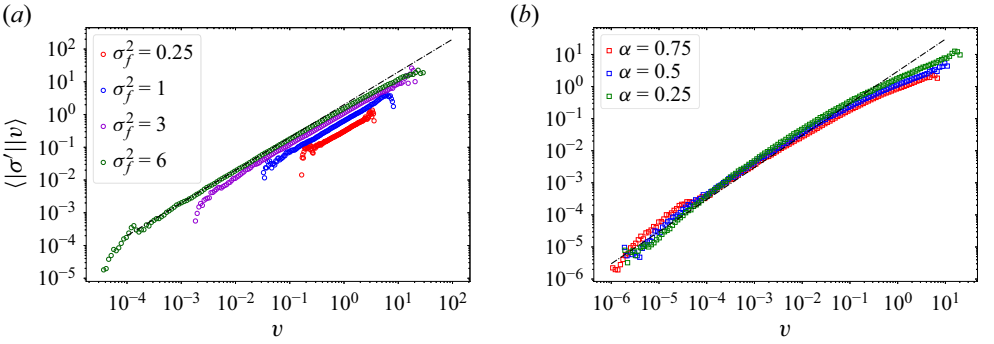


Figure 4. Conditional mean absolute shear rate for (*a*) log-normal distribution of $K(\boldsymbol{x})$ and (*b*) gamma distribution of $K(\boldsymbol{x})$. The dashed lines denote the linear scaling with v.

speeds $v(s)$. The average of $\sigma(s)$ is equal to zero due to the stationarity of the velocity field $\boldsymbol{u}(\boldsymbol{x})$. In order to identify the relation to the speed process, we consider the mean absolute shear rate conditional to the particle speed, $\langle|\sigma||v\rangle$. Figure 4 shows the conditional mean sampled along particle trajectories in log-normal and gamma-distributed conductivity fields. We consistently observe a linear relation between the conditional mean absolute shear rate and velocity, $\langle|\sigma||v\rangle = k_c v$, with k_c a proportionality constant. The inverse of k_c denotes a characteristic shear length scale. Thus, we write $\sigma(s)$ as the following multiplicative process:

$$\sigma(s) = k_c v(s) \xi(s), \tag{3.7}$$

where $\xi(s)$ is a stochastic process with zero mean and unit average $\langle|\xi(s)|\rangle = 1$. Thus, the shear rate is defined entirely by the speed process $v(s)$ and the process $\xi(s)$ defined below. The numerical values for k_c for the log-normal and gamma-distributed conductivity fields under consideration in this work are given in table 1. Note that for the gamma distribution, k_c appears to be constant.

The auxiliary process (3.6) for $\zeta(s)$ thus can be written as

$$\frac{\mathrm{d}\zeta(s)}{\mathrm{d}s} = \frac{k_c \xi(s)}{v(s)^2}. \tag{3.8}$$

Figure 5 shows the PDF of $\xi(s) = \sigma(s)/v(s)k_c$ and illustrates a single $\xi(s)$-trajectory. Its PDF can be well approximated by a Gaussian distribution. Furthermore, its correlation function is approximately exponential and decorrelates on the same scale ℓ_c as the speed process $v(s)$. Thus, we model $\xi(s)$ as the Ornstein–Uhlenbeck process

https://doi.org/10.1017/jfm.2026.12192 Published online by Cambridge University Press

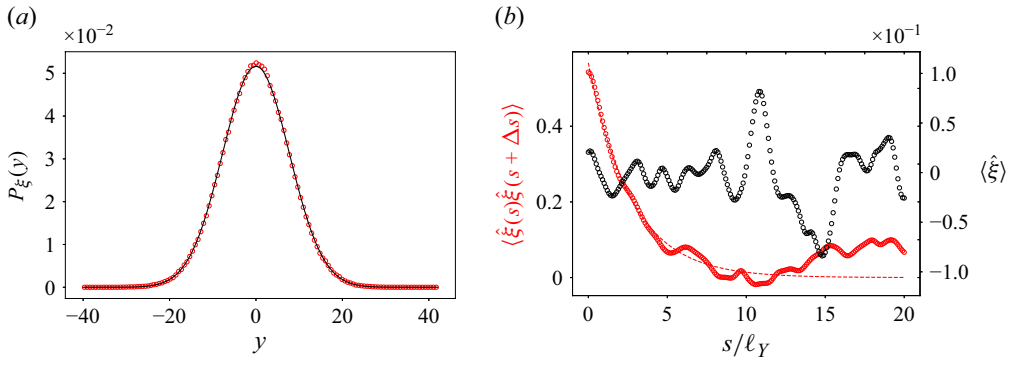


Figure 5. (*a*) (symbols) The PDF of $\xi(s)$ sampled from the numerical simulations and (solid line) the corresponding Gaussian PDF. (*b*) Evolution of $\xi(s)$ in terms of streamline distance and covariance function of $\xi(s)$, which decays on the correlation scale ℓ_c as shown by the red dotted line representing a function proportional to $\exp(-s/\ell_c)$.

$$\frac{\mathrm{d}\xi(s)}{\mathrm{d}s} = -\xi(s)\ell_c^{-1} + \sqrt{\pi\ell_c^{-1}}\eta_2(s). \tag{3.9}$$

The initial values $\xi(s=0) = \xi_0$ are distributed according to

$$p_\xi(y) = \exp\left(-y^2/\pi\right)/\pi, \tag{3.10}$$

which is equal to the stationary distribution of $\xi(s)$. It is Gaussian with the mean absolute value equal to one. Fluid deformation in this framework is obtained from (2.23) by using the stochastic processes for $v(s)$ and $\sigma(s)$ outlined above and projection from $s \to t$ according to (3.1)

$$\ell(t) = |z[s(t)]|. \tag{3.11}$$

The PDF of strip elongations $\ell(t)$ is obtained as

$$p_\ell(l, t) = \langle \delta[l - \ell(t)] \rangle \,. \tag{3.12}$$

3.3. *Summary*

For the convenience of the reader, we summarise the CTRW model for dispersion and stretching of fluid particles. It can be written in differential form as

$$x(s + \mathrm{d}s) = x(s) + \frac{\mathrm{d}s}{\chi}, \quad t(s + ds) = t(s) + \frac{\mathrm{d}s}{v(s)}, \quad v(s) = P_s^{-1}(\phi[w(s)]), \tag{3.13a}$$

$$w(s + \mathrm{d}s) = w(s) - \ell_c^{-1}w(s) + \sqrt{2\ell_c^{-1}\mathrm{d}s}\,Z_1(s), \tag{3.13b}$$

respectively, for particle position, speed and time and

$$z_1(s) = \frac{v(s)}{v(0)}z_1(0) + v(s)v(0)z_2(0)\zeta(s), \quad z_2(s) = \frac{v(0)}{v(s)}z_2(0), \tag{3.13c}$$

$$\zeta(s + ds) = \zeta(s) + \frac{k_c\xi(s)}{v(s)^2}, \quad \xi(s + ds) = \xi(s) + \ell_c^{-1} + \sqrt{\pi\ell_c^{-1}ds}\,Z_2(s), \tag{3.13d}$$

https://doi.org/10.1017/jfm.2026.12192 Published online by Cambridge University Press

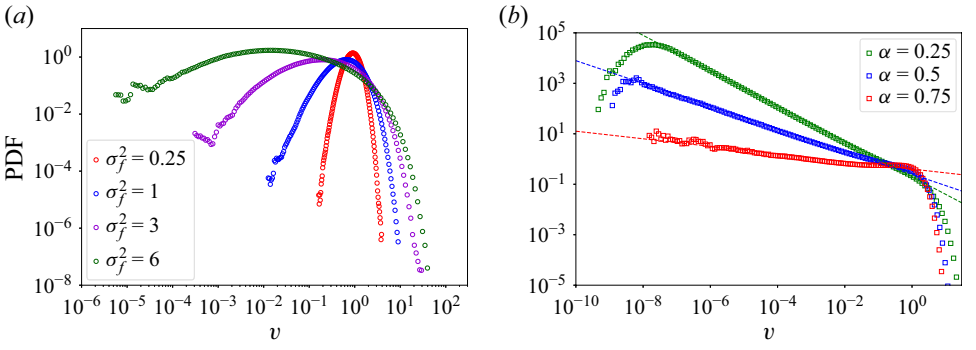


Figure 6. Velocity distributions for (*a*) log-normal fields (*b*) gamma-distributed conductivity fields. The dashed lines in (*b*) denotes the scalings $v^{\beta-1}$ with (top to bottom) $\beta = 0.3, 0.55, 0.85$. Note that the power-law behaviours for the gamma fields are cutoff at a minimum velocity v_m.

for the deformations. The $Z_1(s)$ and $Z_2(s)$ are independent unit Gaussian random variables. The distribution of initial values ξ_0 is given by (3.10). The initial velocity distribution $p_0(v)$ and the distribution of the initial strip orientations are determined by the system under consideration.

3.4. *Discussion of model parameters*

The CTRW framework for dispersion and deformation outlined above uses the Eulerian speed distribution $p_e(v)$, advective tortuosity χ, correlation length ℓ_c and proportionality constant k_c as inputs. The Eulerian speed distribution and advective tortuosity are flow attributes and do not depend on the Lagrangian particle dynamics. For moderately heterogeneous log-normal conductivity fields, it has been found that the speed distribution is also log-normal (Cvetkovic *et al.* 1996). For strongly heterogeneous media, the distribution of low flow speeds can be related to the statistics of low hydraulic conductivities (Fiori *et al.* 2007; Hakoun *et al.* 2019; Hidalgo *et al.* 2022). Figure 6 shows the speed PDFs resulting from the log-normal and gamma-distributed conductivity fields confirming these observations. For the gamma fields, the speed PDFs behave as $p_e(v) \propto v^{\beta-1}$ at small speeds down to a cutoff at around $10^{-7}\langle u \rangle$. The values of the exponent are $\beta = 0.3, 0.55, 0.85$ for $\alpha = 0.25, 0.5, 0.75$. They do not coincide with α, but are consistent with the values observed in Hakoun *et al.* (2019).

The length ℓ_c is the correlation distance of the streamwise Lagrangian speed $v(s)$. It is related to the correlation length ℓ_Y of the multi-Gaussian field $Y(\boldsymbol{x})$ underlying the random conductivity fields $K(\boldsymbol{x})$. Analytical expressions for ℓ_c are only known from perturbation theory for weakly heterogeneous fields (Cvetkovic *et al.* 1996), which gives $\ell_c = 8/3\ell_Y$. For strong heterogeneity, we currently rely on empirical expressions (Cvetkovic *et al.* 1996; Hakoun *et al.* 2019).

As outlined above, the distribution of initial particle speeds and strip orientations depend on the system under consideration. In order to compare the CTRW model with the detailed numerical simulations discussed in Appendix B, the initial speed distribution is set equal to the Eulerian speed PDF, $p_0(v) = p_e(v)$, which corresponds to the uniform initial particle distribution. The distribution for the initial orientation is set equal to the one used for the detailed simulations in the Protean frame given in (B11).

https://doi.org/10.1017/jfm.2026.12192 Published online by Cambridge University Press

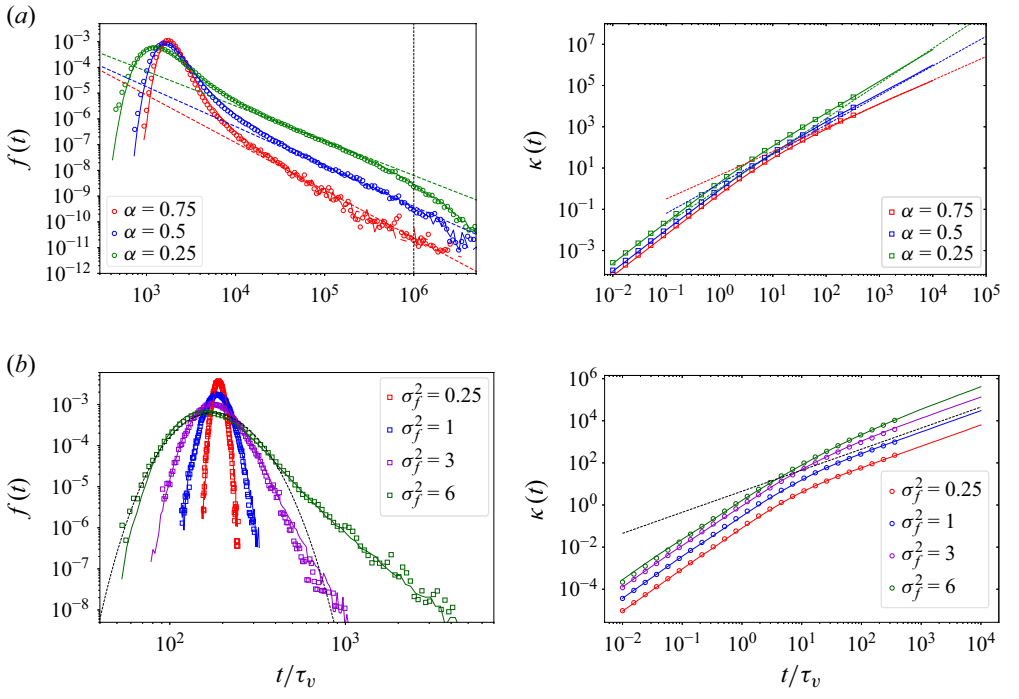


Figure 7. Top panel: (left) First-passage time distribution and (right) displacement variance for the gamma-distributed conductivity fields. The straight dashed lines in the left panel indicate the scalings $t^{-1-\beta}$, and in the right the scalings $t^{2-\beta}$. The power-law scalings are visible in the time regime between the peak time and a cutoff time scale that is given by the lower cutoff velocity in the velocity distribution shown in figure 6, which translates into a cutoff of the particle transition times at around $10^6\tau_v$. Bottom panel: The same for the log-normal conductivity fields. The symbols denote the data from the detailed numerical simulations, the straight lines the CTRW model. The black dashed line in the left panel denotes the fit of the data for $\sigma f^2 = 6$ with an inverse Gaussian distribution, the analytical solution of the advection–dispersion equation with constant velocity and longitudinal dispersion coefficient. The black dashed line in the right panel denotes the asymptotic linear scaling of the displacement variances at large times.

4. How porous medium heterogeneity controls stirring

We study here how the porous medium heterogeneity controls stirring. To this end, we consider detailed numerical simulations of the stretching and dispersion behaviours in the heterogeneous hydraulic conductivity fields given in § 2.1. The medium heterogeneity is characterised by the $K(\boldsymbol{x})$ statistic, which is mapped through the flow equation (2.2) onto the flow velocity $\boldsymbol{q}(\boldsymbol{x})$. We analyse here how the observed dispersion and stretching behaviours can be related to the medium heterogeneity in terms of the distribution of Eulerian flow velocities using the CTRW model presented in § 3. Note that the dispersion behaviours for this type of conductivity field was discussed in depth in Comolli *et al.* (2019). Thus, here we focus on stretching. We present the dispersion behaviour for completeness and to demonstrate the capability of the CTRW model of § 3 to quantify and predict both dispersion and stretching.

4.1. *Dispersion*

Figure 7 shows the first-passage time distributions and displacement variances for particle motion in gamma-distributed and log-normal conductivity fields and their estimates based on the CTRW model. For both scenarios, the CTRW model provides an excellent

https://doi.org/10.1017/jfm.2026.12192 Published online by Cambridge University Press

description of the direct numerical data. It reproduces all non-Fickian transport features and shows the link between the particle dispersion and the medium heterogeneity in terms of the Eulerian velocity field.

In order to further analyse the observed scalings and non-Fickian dispersion features, we first note that particle velocities are independent for separation distances larger than ℓ_c and vary only weakly for distances larger than ℓ_c. Thus, the equations of motion (3.13*a*) of a particle can be coarse grained as

$$x_{n+1} = x_n + \frac{\ell_c}{\chi}, \qquad t_{n+1} = t_n + \tau_n, \qquad \tau_n = \frac{\ell_c}{v_n}, \tag{4.1}$$

where the v_n are independent random velocities. For the uniform initial particle distribution under consideration here, the initial particle speeds v_0 are distributed according to $p_e(v)$. For all subsequent steps, they are distributed according to $p_s(v)$, which is defined in terms of $p_e(v$ by (2.13). The PDF of transition times τ_n for $n > 0$ is denoted by $\psi(t)$, which can be expressed in terms of the Eulerian speed distribution by

$$\psi(t) = \frac{\tau_c \ell_c}{t^3} p_e(\ell_c/t), \tag{4.2}$$

where we defined $\tau_c = \ell_c/\langle u \rangle$. The initial transition times $\tau_0 = \ell_c/v_0$ are given accordingly by

$$\psi_0(t) = \frac{\ell_c}{t^2} p_e(\ell_c/t). \tag{4.3}$$

In this coarse-grained framework, the first-passage time of a particle at a distance $x_n = n\ell_c/\chi$ is given by

$$t_n = \tau_0 + \sum_{i=1}^{n-1} \tau_i. \tag{4.4}$$

That is, the first-passage times are the sums of independent random transition times. Their distribution is given by the convolution of $\psi_0(t)$ and the $n-1$-fold convolution of $\psi(t)$. Thus, the scaling of the first-passage time distribution can be understood in terms of the scaling of the transition time distribution, and thus, in terms of the velocity distributions.

For the gamma fields, the Eulerian velocity distribution scales as $p_e(v) \propto v^{\beta-1}$ with $0 < \beta < 1$ for velocities in the interval $v_m \ll v \ll \langle u \rangle$, that is, between a lower cutoff velocity v_m and the mean velocity $\langle u \rangle$; see figure 6. Thus, the initial transition time distribution scales as $\psi_0(t) \sim t^{-1-\beta}$ for $\tau_c \ll t \ll \tau_m$, while the transition time distributions for all subsequent steps scale as $\psi(t) \sim t^{-2-\beta}$. That is, $\psi_0(t)$ has a stronger tail behaviour than $\psi(t)$, and thus it dominates the tail behaviour of the first-passage time distribution, which scales as $f(t, x_1) \propto t^{-1-\beta}$ for $t \ll \tau_m$. The power-law tails are cutoff at times of around $\tau_m = \ell_c/v_m \approx 10^6 \tau_v$. The displacement means for the gamma fields (not shown) are evolving linearly with time and are equal to $\mu(t) = \langle u \rangle t$. The displacement variance evolves ballistically at short times $t < \tau_v$, and according to a power law at increasing time. The CTRW theory predicts the behaviour $\kappa(t) \propto t^{2-\beta}$ for $\tau_c \ll t \ll \tau_m$ (Comolli *et al.* 2019); see figure 7(*a*).

For the log-normal conductivity fields, the first-passage time distributions do not display heavy tails for small $\sigma_f^2 \leqslant 1$; see figure 7(*b*). For larger σ_f^2, we observe strong tailing, which again can be traced back to the broad distribution of Eulerian flow speeds, which displays power-law tangents over more than one order of magnitude for intermediate values of v. The displacement mean evolves as $\mu(t) = \langle u \rangle t$. The displacement variance shows ballistic

https://doi.org/10.1017/jfm.2026.12192 Published online by Cambridge University Press

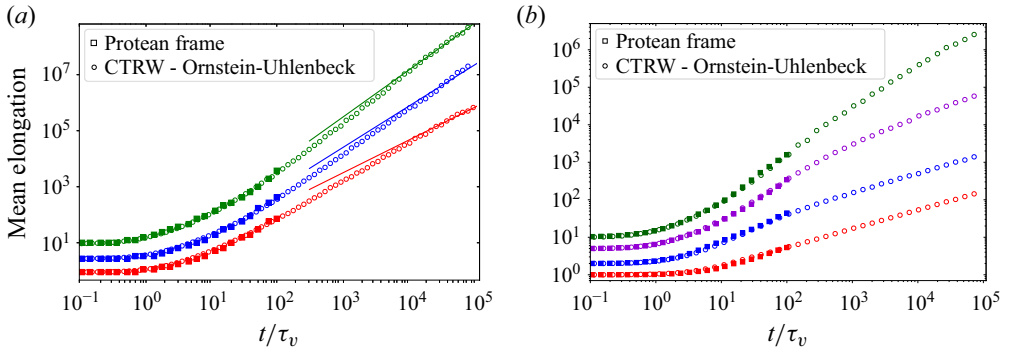


Figure 8. Mean strip elongation for (left) gamma and (right) log-normal conductivity fields. Full symbols denote the detailed numerical simulations, open symbols the CTRW model. The solid lines in the left panel denote the power-law scaling obtained from the Lévy walk model (4.8) for the stretching evolution. The asymptotic scaling is reached at around $10^4\tau_v$. The elongation data are multiplied by multiples of 5 in the left panel and by multiples of 5/2 in the right panel for clearer illustration. The colour code is the same as in figure 7.

behaviour at early times and then crosses over toward a linear long-time scaling. For $\sigma_f^2 = 3$ and 6, there is a broad power-law cross-over, which originates in the broad distribution of flow speeds shown in figure 6. While the displacement variance asymptotically tends toward Fickian, that is, linear scaling for all σ_f^2, the first-passage time distribution may still display heavy tailed behaviour. This is illustrated in figure 7(*b*) for the case $\sigma_f^2 = 6$. The dashed black line denotes the fit of an inverse Gaussian distribution ((11) in Kreft & Zuber (1978)) with constant velocity and longitudinal dispersion coefficient. While the bulk behaviour is well represented by the analytical solution, the tail behaviour cannot be captured.

4.2. *Stretching*

In the previous section, we have seen, how the medium heterogeneity impacts on particle dispersion and how this can be quantified in terms of the CTRW model. In this section, we analyse the stretching behaviours in the gamma and log-normal conductivity fields in terms of the mean elongation of a material strip and the PDF of strip elongations. In order to link the stretching behaviour to the medium heterogeneity, we use the CTRW model presented in § 3.

Figure 8 shows the evolution of the mean elongation $\lambda(t)$ for the gamma and log-normal conductivity fields obtained using Protean coordinates, as outlined in Appendix B.3. The data from the detailed numerical model are compared with the estimates from the CTRW model presented in § 3. The CTRW model is able to describe all the salient features of the evolution of the mean elongation in terms of only the Eulerian speed distribution. It provides a direct link between medium and flow heterogeneity and the stretching behaviour. In the following, the observed stretching behaviours are discussed in more detail in the light of this relation.

At early times, the evolution of $\ell(t)$ is linear, which can be understood by considering equations (2.22), and noting that, at times $t \ll \tau_c$, particle speeds and shear rates can be considered constant and equal to their initial values v_0 and σ_0. Inserting these short-time approximations into (2.22) gives

$$z_1(t) = \delta a_1 + \delta a_2 \sigma_0 t, \qquad z_2(t) = \delta a_2. \tag{4.5}$$

https://doi.org/10.1017/jfm.2026.12192 Published online by Cambridge University Press

Thus, the short time evolution of the strip elongation $\ell(t) = \sqrt{z_1(t)^2 + z_2(t)^2}$ is given by

$$\ell(t) = \sqrt{(\delta a_1 + \delta a_2 \sigma_0 t)^2 + \delta a_2^2} = \ell_0 + \frac{\delta a_1 \delta a_2}{\ell_0} \sigma_0 t + \cdots , \tag{4.6}$$

where the dots denote higher-order contributions. Hence, the early time behaviour is linear.

For increasing times, the mean elongation crosses over to a power-law behaviour as

$$\lambda(t) \propto t^{\gamma}, \tag{4.7}$$

where γ is a scaling exponent that is specified in the following. In order to assess the long-time evolution of fluid deformation, Dentz *et al.* (2016*b*) formulated the stretching process as a coupled CTRW or Lévy walk. In fact, and as outlined in § 4.1, for separation distances larger than the correlation length ℓ_c, subsequent particle speeds can be considered independent, while the particle velocities vary only weakly for distances smaller than ℓ_c. In analogy to the coarse graining of the particle motion, we coarse grain the deformation process on the scale ℓ_c and write (3.8) as

$$\zeta_{n+1} = \zeta_n + k_c \ell_c^{-1} \sqrt{\pi} \xi_n \tau_n^2, \qquad t_{n+1} = t_n + \tau_n. \tag{4.8}$$

The ξ_n values are independent unit Gaussian random variables. The process (4.8) denotes a coupled CTRW, and for a power-law distribution of transition times, a Lévy walk (Zaburdaev *et al.* 2015; Dentz *et al.* 2015). The coupling is expressed by the fact that the increment of the ζ_n process is proportional to the square of the time increment τ_n. The strip elongation after n random walk steps is then given by

$$\ell_n = \sqrt{\left[\frac{v_n}{v_0} z_1(0) + v_n z_2(0) \zeta_n\right]^2 + \left[\frac{v_0}{v_n} z_2(0)\right]^2}. \tag{4.9}$$

In the limit of large ζ_n one can expand this expression, and one obtains for the strip elongation at leading order

$$\ell_n = v_n v_0 \delta a_2 |\zeta_n|, \tag{4.10}$$

where we used the fact that $z_2(0) = \delta a_2$. Thus, the evolution of the strip elongation can be rationalised in terms of the Lévy walk (4.8). This coarse-grained picture is valid for travel distances much larger than ℓ_c, or equivalently for times much larger than τ_c.

The power-law behaviour given by (4.7) can now be understood on the basis of the Lévy walk (4.8) and the scalings derived in Rebenshtok *et al.* (2014) and Dentz *et al.* (2015). Recall that the distribution of transition times $\psi(t)$ exhibits the power-law behaviour $\psi(t) \propto t^{-2-\beta}$ for $\tau_c \ll t \ll \tau_m$, as outlined in § 4.1. Dentz *et al.* (2015) show that, for $0 < \beta < 1$, which is the case for the gamma fields, Lévy walk theory predicts that the scaling exponent in (4.7) is equal to $\gamma = 2 - \beta$. The data for $\lambda(t)$ from the detailed numerical simulations and the CTRW model agree with these theoretical scalings. For the log-normal conductivity fields, the Eulerian speed PDFs do not exhibit a clear scaling at small speeds. The scaling behaviours for the elongation in this case fall into the class defined by $\beta > 3$. In this case, Lévy walk theory predicts the scaling exponent $\gamma = 1/2$ (Dentz *et al.* 2015). At intermediate times, power-law cross-overs can be observed that are related to power-law tangents in the speed PDF.

The distribution of strip elongations $p_\ell(l, t)$ plays a central role for the quantification of the concentration content of a disperse mixture (Le Borgne *et al.* 2013, 2015). Regions of strong stretching lead to a fast decay of solute concentrations by diffusion, because stretching leads to a steepening of concentration gradients. This dynamics is quantified by the diffusive strip method (Villermaux 2019), which allows us to map the elongation PDF directly on the PDF of concentration point values.

https://doi.org/10.1017/jfm.2026.12192 Published online by Cambridge University Press

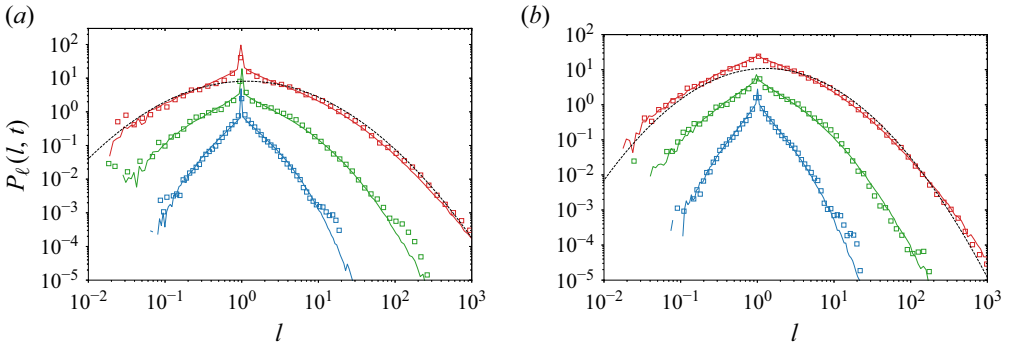


Figure 9. The PDFs of strip elongations for (*a*) gamma fields for $\alpha = 0.25$ and (*b*) log-normal conductivity fields for $\sigma_f^2 = 6$ at times $t = 1, 5, 20\tau_c$. The symbols denote the detailed numerical simulations, the solid lines the CTRW model and the dash-dotted lines fits of the log-normal distribution for $t = 20\tau_c$. The PDFs are shifted along the vertical axis by multiplication with a constant factor to avoid overlap.

Figure 9 shows the PDF $p_\ell(l, t)$ for the gamma and log-normal fields for the strongest heterogeneities with $\alpha = 0.25$ and $\sigma_f^2 = 6$ at different times. The Supplementary Information provides the results for the elongation PDFs for all the analysed hydraulic conductivity fields. The CTRW model is in excellent agreement with the data from the detailed numerical simulations at all observation times. At short times, $p_\ell(l, t)$ the PDF is sharply peaked at the initial elongation. At increasing times, it becomes skewed toward larger values of elongation following the coupled CTRW process, and the peak is smoothed

These results show how the medium heterogeneity impacts on and controls the elongation and thus the stretching behaviour. Both the mean elongation and its distribution can be linked to the medium heterogeneity via the CTRW model.

4.3. *Discussion*

The way porous media stir a fluid is very different from the way chaotic or turbulent flows stir a free fluid. We are considering Darcy-scale flow, that is, the bulk fluid is stirred by the spatial variability as it is permeating through the medium driven by a pressure gradient. The ensuing spatial variability of the steady flow field leads to the deformation of a material line as shown in figure 3, and the dispersion of solute fronts. Furthermore, material strips experience a series of deformation events, stretching and compression, as they are transported along the streamlines of the bulk flow, also shown in figure 3. Steady isotropic Darcy is special in the sense that chaotic flow is prohibited (Lester *et al.* 2022), and thus stretching is sub-exponential, and in general characterised by power-law stretching behaviours, as shown in the previous section. The works by Le Borgne *et al.* (2013) and Le Borgne *et al.* (2015) proposed to model the evolution of strip elongation as a multiplicative stochastic process with coefficients whose time dependence is adjusted from the elongation data so as to match the observed mean elongation behaviour. This framework predicts the PDF of elongation to be log-normal. As shown in figure 9, the PDF is not log-normal at times smaller than $20\tau_c$. For $t = 20\tau_c$ a log-normal distribution provides a reasonable approximation of the data. However, this modelling approach is based on a stochastic dynamics that is obtained by fitting the stretching time series as a geometric Brownian motion, and therefore it does not provide a link between the stretching behaviour and medium heterogeneity

https://doi.org/10.1017/jfm.2026.12192 Published online by Cambridge University Press

In this paper, we have taken a different route with the aim of understanding and quantifying how the medium heterogeneity stirs the bulk fluid and how it controls the stretching behaviour. This implies the formulation of the stretching problem in Protean coordinates aligned with the streamlines of the flow in § 2.3. This framework reveals the dynamics of stretching that results from the topological constraints of steady Darcy flow. It shows that stretching is dominated by the series of shear deformations of variable durations that a strip experiences as it is transported through the heterogeneous medium. The duration of shear episodes varies because the residence or transition times of a material strip vary according to the local flow velocity. This formulation allows for a first-principles derivation of the stochastic stretching model in § 3. The model belongs to the class of CTRWs, which naturally reflects the fact that flow and, in this case, stretching, are organised along the spatial structure imprinted in the hydraulic conductivity distribution. In § 4, this model is used to quantitatively link the observed dispersion and stretching behaviours to the Eulerian velocity distribution.

5. Summary and conclusions

We study the mechanisms and stochastic dynamics of stretching and dispersion of fluid elements in heterogeneous two-dimensional porous media. We consider the quantitative link between stretching and dispersion on the one hand, and between the stretching behaviour and the medium and flow properties on the other. This leads to an upscaled modelling approach and identification of the key parameters to predict both large-scale fluid deformation and dispersion, which are key inputs for mixing models in porous media (Villermaux 2019).

In order to identify the stochastic dynamics of fluid deformation, we first formulate the deformation problem in Protean coordinates that are aligned along streamlines. This formulation reveals the key role played by the Lagrangian series of particle speeds and shear rates for the evolution of the elongation of a fluid material strip. We focus on particle speeds and shear rates sampled equidistantly along streamlines, which reflect the spatial organisation of the steady flow fields. Their stochastic evolutions are quantified through stationary Markov processes. Both are characterised by a single correlation length scale. Following the CTRW approach for particle dispersion, the speed process is represented by an Ornstein–Uhlenbeck process for the normal score transform of particle speeds. For the shear rate process, we find that (i) it is linearly correlated to the particle speed, (ii) that its conditional distribution is Gaussian and (iii) that it evolves on the same correlation scale as the speed process. Based on these findings, we model the stochastic evolution of shear rates also as an Ornstein–Uhlenbeck process. This CTRW formulation renders a single stochastic framework for the quantification and analysis of dispersion and fluid deformation.

The framework is employed to analyse deformation of fluid particles obtained from direct numerical simulations in gamma-distributed and log-normal hydraulic conductivity fields. Our analysis confirms existing results for dispersion in terms of first-passage time distributions and displacement moments. We observe common signatures of non-Fickian dispersion, such as a broad distribution of first-passage times and nonlinear evolutions of the displacement variance. These non-Fickian features are also reflected by the mean elongation of material strips, which is a measure of stretching. The initially linear behaviour evolves toward asymptotic power-law scalings that are determined by the behaviour of the Eulerian speed PDF. These behaviours are fully predicted by the derived CTRW stretching model in terms of the Eulerian speed PDF. The observed scalings are related analytically to the scalings of the speed PDF by noting that the coarse-grained

https://doi.org/10.1017/jfm.2026.12192 Published online by Cambridge University Press

deformation process follows a coupled CTRW, or, in the case of power-law distributions of particle transition times, a Lévy walk. In summary, the derived CTRW model predicts the stretching and dispersion behaviour in terms of the Eulerian speed PDF and thus elucidates how the medium heterogeneity controls stirring.

The understanding of the heterogeneity controls on stretching is central for the quantification and prediction of mixing and chemical reactions in porous media (Villermaux 2019; Rolle & Le Borgne 2019). Stretching of a material strip leads to strong concentration gradients in the direction perpendicular to it, which accelerate mixing and chemical reactions. In a heterogeneous porous medium, regions of strong stretching are related to reaction hotspots (Rolle & Le Borgne 2019), which can explain dissolution and precipitation patterns in porous media (Hidalgo *et al.* 2015; Cil *et al.* 2017; Kottsova *et al.* 2025) and give insight into karst formation (De Vriendt *et al.* 2020) and the spatial distribution of ore deposits, which are typically located along structures that promote mixing.

Supplementary material. Supplementary material are available at https://doi.org/10.1017/jfm.2026.12192.

Acknowledgements. K.F., J.J.H. and M.D. acknowledge funding from the European Union's Horizon 2020 research and innovation program under the Marie Sklodowska-Curie grant agreement Number 956457 through the project CoPerMix.

Declaration of Interests. The authors report no conflict of interest.

Appendix A. Transformation of the velocity gradient tensor into Protean coordinates

In order to derive (2.18), we take the time derivative of (2.16), which is given by

$$\frac{\mathrm{d}z'}{\mathrm{d}t} = \frac{\mathrm{d}}{\mathrm{d}t}\left[\boldsymbol{A}^T(t)\boldsymbol{z}(t)\right] = \frac{\mathrm{d}\boldsymbol{A}^T}{\mathrm{d}t}\boldsymbol{z}(t) + \boldsymbol{A}^T(t)\frac{\mathrm{d}\boldsymbol{z}(t)}{\mathrm{d}t}. \tag{A1}$$

Using (2.14) gives

$$\frac{\mathrm{d}z'}{\mathrm{d}t} = \frac{\mathrm{d}\boldsymbol{A}^T}{\mathrm{d}t}\boldsymbol{z}(t) + \boldsymbol{A}^T(t)\boldsymbol{\epsilon}(t)\boldsymbol{z}(t) = \left[\frac{\mathrm{d}\boldsymbol{A}^T}{\mathrm{d}t} + \boldsymbol{A}^T(t)\boldsymbol{\epsilon}(t)\right]\boldsymbol{z}(t). \tag{A2}$$

Using that $\boldsymbol{z}(t) = \boldsymbol{A}(t)\boldsymbol{z}'(t)$ gives

$$\frac{\mathrm{d}z'}{\mathrm{d}t} = \left[\frac{\mathrm{d}\boldsymbol{A}^T}{\mathrm{d}t} + \boldsymbol{A}^T(t)\boldsymbol{\epsilon}(t)\right]\boldsymbol{A}(t)\boldsymbol{z}'(t) = \left[\frac{\mathrm{d}\boldsymbol{A}^T}{\mathrm{d}t}\boldsymbol{A}(t) + \boldsymbol{A}^T(t)\boldsymbol{\epsilon}(t)\boldsymbol{A}(t)\right]\boldsymbol{z}'(t). \tag{A3}$$

The expression in the square brackets on the right side defines the transformed velocity gradient in (2.18).

Appendix B. Numerical simulations

B.1 *Field generation and flow simulations*

As outlined in § 2.1, the hydraulic conductivity fields are generated by transformation from a Gaussian-distributed multi-Gaussian random field $Y(\boldsymbol{x})$. The latter is generated using the fast Fourier transform following Ruan & McLaughlin (1998) on a two-dimensional computational domain that is discretised into $N = 1000 \times 2000$ nodes in directions transverse and longitudinal to the mean flow. The method assures periodicity in both directions. The domain dimensions are $100\ell_Y \times 200\ell_Y$. We generate $N_R = 200$ realisations of each random field.

https://doi.org/10.1017/jfm.2026.12192 Published online by Cambridge University Press

The conductivity fields with a log-normal marginal distribution are generated from $Y(\boldsymbol{x})$ according to (2.7). In the numerical simulations, we set $\mu_f = 0$ and probe different values for σ_f^2. For the gamma fields, there is no analytical map, because there is no closed form expression for the inverse of the cumulative gamma distribution. Here, we use a gamma distribution that is truncated from below at k_{min}. Thus, its cumulative distribution is given by

$$P_K(k) = \frac{P_\Gamma(k) - P_\Gamma(k_{min})}{1 - P_\Gamma(k_{min})}, \tag{B1}$$

where $P_\Gamma(k)$ is the CDF of the gamma distribution

$$p_\Gamma(k) = \left(\frac{k}{k_0}\right)^{\alpha-1} \frac{\exp(-k/k_0)}{\Gamma(\alpha)k_0}. \tag{B2}$$

For the numerical mapping using the Smirnov transform, conductivity values are organised in logarithmically spaced bins. The values of the exponent α are chosen to be between zero and one. Furthermore, we set $k_0 = 1/\alpha$ and $k_{min} = 10^{-5}k_0$ so that the arithmetic mean conductivity is approximately one.

The flow equation (2.2) is solved using a finite volume method based on a two-point flux approximation, as described in Aarnes *et al.* (2007). The mean flow velocity $\langle u \rangle$ is imposed along the 1-direction. The advective time is thus defined as $\tau_v = \ell_Y / \langle u \rangle$. In the perpendicular directions, periodic boundary conditions are imposed for hydraulic head. This scheme on a regular grid is equivalent to a finite difference scheme. It provides the hydraulic head at the cell centres and the flow velocities perpendicular to the cell faces. In order to determine the local velocity gradient the flow field is interpolated by a third-order spline for the velocity components $u_1(\boldsymbol{x})$ and $u_2(\boldsymbol{x})$. Figure 2 illustrates the hydraulic conductivity distribution and the resulting Darcy flow field.

B.2 *Displacement moments and first-passage times*

For the numerical calculation of displacement moments and first-passage time distributions, we use the Pollock method (Pollock 1988) to numerically integrate the kinematic equation (2.10). Particles are injected uniformly along a straight line perpendicular to the mean flow direction. The line is located at a distance of $5\ell_Y$ from the left domain boundary to avoid boundary effects and represents 90% of the perpendicular length of the domain.

The longitudinal displacement mean and variance are determined from the particle positions by averaging of $N_p = 10^4$ particles in $N_R = 200$ medium realisations

$$\mu(t) = \frac{1}{N_R}\sum_{i=1}^{N_R}\frac{1}{N_p}\sum_{j=1}^{N_p} x_1^{(i,j)}(t), \quad \kappa(t) = \frac{1}{N_R}\sum_{i=1}^{N_R}\frac{1}{N_p}\sum_{j=1}^{N_p}\left[x_1^{(i,j)}(t) - \mu(t)\right]^2, \tag{B3}$$

where $x_1^{(i,j)}(t)$ denotes the longitudinal position of the jth particle in the ith disorder realisation. The first-passage times are determined according to (2.26) by the minimum time a particle needs to arrive at the control plane perpendicular to the mean flow direction. The PDF of first-passage times is determined by

$$f(t, x_1) = \frac{1}{N_R}\sum_{i=1}^{N_R}\frac{1}{N_p}\sum_{j=1}^{N_p}\sum_{k=1}^{N_b}\frac{\mathbb{I}(t_i \leqslant \tau^{(i,j)}(x_1) \leqslant t_{k+1})}{t_{k+1} - t_k}, \tag{B4}$$

https://doi.org/10.1017/jfm.2026.12192 Published online by Cambridge University Press

where $\tau^{(i,j)}$ denotes the first-passage time of particle j in realisation i, $\mathbb{I}(\cdot)$ is the indicator function, which is one if its argument is true and zero else, and the t_k values are the edges of the time bins to determine the numerical histogram. Due to the broad range of first-passage times, we use a logarithmic binning.

B.3 *Lagrangian fluid deformation*

The numerical calculation of fluid deformation is based on formulation (2.23) in the Protean coordinate frame, in combination with particle tracking in streamline distance s as expressed by (2.12). We use an Euler forward scheme to integrate the latter

$$x_1(s_k + \Delta s) = x_1(s_k) + \frac{v_1(s_k)\Delta s}{v(s_k)}, \tag{B5}$$

$$x_2(s_k + \Delta s) = x_2(s_k) + \frac{v_2(s_k)\Delta s}{v(s_k)}, \tag{B6}$$

$$t(s_k + \Delta s) = t(s_k) + \frac{\Delta s}{v(s_k)}, \tag{B7}$$

with $s_k = k\Delta s$ and $\Delta s = 10^{-2}\ell_Y$. The system (2.23) is discretised accordingly. It can be written as

$$z_1(s_k) = \frac{v(s_k)}{v(0)} z_1(0) + v(s_k)v(0)\zeta(s_k), \tag{B8}$$

$$z_2(s_k) = \frac{v(0)}{v(s_k)} z_2(0), \tag{B9}$$

where $\zeta(s_k)$ represents the integral term on the right side of (2.23*a*). It is evaluated by the trapezoidal rule as

$$\zeta(s_k) = \frac{\Delta s}{2}\left[\frac{\sigma(0)}{v(0)^3} + \frac{\sigma(s_k)}{v(s_k)^3}\right] + \sum_{n=1}^{s_{k-1}} \Delta s \frac{\sigma(s_n)}{v(s_n)^3}. \tag{B10}$$

The initial values $z_1(0)$ and $z_2(0)$ are

$$z_1(0) = \ell_0 \cos(\theta), \qquad z_2(0) = \ell_0 \sin(\theta), \tag{B11}$$

where the angle θ is drawn from a Gaussian distribution with mean $\pi/2$ and variance one. The observables at a given time t are obtained by projecting step number k onto time through $k_t = \max[k|t(s_k) \leqslant t]$

$$\boldsymbol{z}(t) = \boldsymbol{z}(s_{k_t}). \tag{B12}$$

Furthermore, we use a two-particle method, which numerically calculates the distance vector $\boldsymbol{z}(t) = \boldsymbol{x}(t, \boldsymbol{a}) - \boldsymbol{x}(t, \boldsymbol{a} + \delta\boldsymbol{a})$ between two particles that are initially spaced by $\ell_0 = |\delta\boldsymbol{a}| = 10^{-5}\ell_Y$. The particle positions are determined by the Pollock method (Pollock 1988). The particle pairs are placed along a line perpendicular to the mean flow direction at a distance of $5\ell_Y$ from the left domain boundary. The initial orientation is chosen consistent with (B11) as

$$\boldsymbol{z}(t = 0) = \boldsymbol{A}(0)\boldsymbol{z}(s = 0), \tag{B13}$$

where $\boldsymbol{A}(0)$ is defined by (2.15).

https://doi.org/10.1017/jfm.2026.12192 Published online by Cambridge University Press

References

Aarnes, J.E., Gimse, T. & Lie, K.-A. 2007 An introduction to the numerics of flow in porous media using matlab. In *Geometric Modelling, Numerical Simulation, and Optimization: Applied Mathematics at SINTEF* (ed. G. Hasle, K.-A. Lie & E. Quak), pp. 265–306. Springer.

Adachi, K. 1983 Calculation of strain histories in protean coordinate systems. *Rheol. Acta* **22** (4), 326–335.

Adams, E.E. & Gelhar, L.W. 1992 Field study of dispersion in a heterogeneous aquifer: 2. Spatial moments analysis. *Water Resour. Res.* **28** (12), 3293–3307.

Ashurst, W.T., Kerstein, A.R., Kerr, R.M. & Gibson, C.H. 1987 Alignment of vorticity and scalar gradient with strain rate in simulated Navier–Stokes turbulence. *Phys. Fluids* **30** (8), 2343–2353.

Attinger, S., Dentz, M. & Kinzelbach, W. 2004 Exact transverse macro dispersion coefficients for transport in heterogeneous porous media. *Stoch. Environ. Res. Risk Assessm.* **18** (1), 9–15.

Bear, J. 1972 *Dynamics of Fuids in Porous Media*. American Elsevier.

Berkowitz, B., Cortis, A., Dentz, M. & Scher, H. 2006 Modeling non-fickian transport in geological formations as a continuous time random walk. *Rev. Geophys.* **44**, RG2003.

Cil, M.B., Xie, M., Packman, A.I. & Buscarnera, G. 2017 Solute mixing regulates heterogeneity of mineral precipitation in porous media. *Geophys. Res. Lett.* **44** (13), 6658–6666.

Cocke, W.J. 1969 Turbulent hydrodynamic line stretching: consequences of isotropy. *Phys. Fluids* **12** (12), 2488–2492.

Comolli, A., Hakoun, V. & Dentz, M. 2019 Mechanisms, upscaling and prediction of anomalous dispersion in heterogeneous porous media. *Water Resour. Res.* **55**, 8197–8222.

Cvetkovic, V., Cheng, H. & Wen, X.-H. 1996 Analysis of nonlinear effects on tracer migration in heterogeneous aquifers using lagrangian travel time statistics. *Water Resour. Res.* **32** (6), 1671–1680.

Dagan, G. 2012 *Flow and Transport in Porous Formations*. Springer Science & Business Media.

De Vriendt, K., Pool, M. & Dentz, M. 2020 Heterogeneity-induced mixing and reaction hot spots facilitate karst propagation in coastal aquifers. *Geophys. Res. Lett.* **47** (10), e2020GL087529.

Dentz, M. & Hyman, J.D. 2023 The hidden structure of hydrodynamic transport in random fracture networks. *J. Fluid Mech.* **977**, A38.

Dentz, M., Kang, P.K., Comolli, A., Le Borgne, T. & Lester, D.R. 2016*a* Continuous time random walks for the evolution of Lagrangian velocities. *Phys. Rev. Fluids* **1** (7), 074004.

Dentz, M., Le Borgne, T., Lester, D.R. & de Barros, F.P.J. 2015 Scaling forms of particle densities for lévy walks and strong anomalous diffusion. *Phys. Rev. E* **92** (3), 032128.

Dentz, M., Lester, D.R., Le Borgne, T. & de Barros, F.P.J. 2016*b* Coupled continuous-time random walks for fluid stretching in two-dimensional heterogeneous media. *Phys. Rev. E* **94** (6), 061102.

Dentz, M. & Massoudieh, A. 2025 Linear boltzmann equation for solute dispersion in heterogeneous media under non-ergodic conditions. *ARC Geophys. Res.* **1** (1), 4.

Devroye, L. 1986 *Non-Uniform Random Variate Generation*. Springer-Verlag.

Doob, J.L. 1942 The Brownian movement and stochastic equations. *Ann. Math.* **43** (2), 351–369.

de Dreuzy, J.-R., Beaudoin, A. & Erhel, J. 2007 Asymptotic dispersion in 2D heterogeneous porous media determined by parallel numerical simulations. *Water Resour. Res.* **43** (10), W10439.

Fiori, A., Janković, I. & Dagan, G. 2003 Flow and transport in highly heterogeneous formations: 2. Semianalytical results for isotropic media. *Water Resour. Res.* **39** (9), 1269.

Fiori, A., Janković, I., Dagan, G. & Cvetković, V. 2007 Ergodic transport through aquifers of non-gaussian log conductivity distribution and occurrence of anomalous behavior. *Water Resour. Res.* **43** (9), W09407.

Frippiat, C.C. & Holeyman, A.E. 2008 A comparative review of upscaling methods for solute transport in heterogeneous porous media. *J. Hydrol.* **362** (1–2), 150–176.

Gelhar, L.W. 1993 *Stochastic Subsurface Hydrology*. Prentice-Hall.

Gelhar, L.W. & Axness, C.L. 1983 Three-dimensional stochastic analysis of macrodispersion in aquifers. *Water Resour. Res.* **19** (1), 161–180.

Gotovac, H., Cvetkovic, V. & Andricevic, R. 2009 Flow and travel time statistics in highly heterogeneous porous media. *Water Resour. Res.* **45** (7), W07402.

Gómez-Hernández, J.J. & Wen, X.-H. 1998 To be or not to be multi-Gaussian? A reflection on stochastic hydrogeology. *Adv. Water Resour.* **21** (1), 47–61.

Hakoun, V., Comolli, A. & Dentz, M. 2019 Upscaling and prediction of lagrangian velocity dynamics in heterogeneous porous media. *Water Resour. Res.* **55** (5), 3976–3996.

Heyman, J., Lester, D.R., Turuban, R., Méheust, Y. & Le Borgne, T. 2020 Stretching and folding sustain microscale chemical gradients in porous media. *Proc. Natl Acad. Sci.* **117** (24), 13359–13365.

Hidalgo, J.J., Dentz, M., Cabeza, Y. & Carrera, J. 2015 Dissolution patterns and mixing dynamics in unstable reactive flow. *Geophys. Res. Lett.* **42** (15), 6357–6364.

https://doi.org/10.1017/jfm.2026.12192 Published online by Cambridge University Press

HIDALGO, J.J., NEUWEILER, I. & DENTZ, M. 2022 Advective trapping in the flow through composite heterogeneous porous media. *Transport Porous Med.* **143** (3), 599–618.
HYMAN, J.D. & DENTZ, M. 2021 Transport upscaling under flow heterogeneity and matrix-diffusion in three-dimensional discrete fracture networks. *Adv. Water Resour.* **155**, 103994.
KANG, P.K., LE BORGNE, T., DENTZ, M., BOUR, O. & JUANES, R. 2015 Impact of velocity correlation and distribution on transport in fractured media: field evidence and theoretical model. *Water Resour. Res.* **51** (2), 940–959.
KELLER, J.B. 1964 A theorem on the conductivity of a composite medium. *J. Math. Phys.* **5** (4), 548–549.
KOTTSOVA, A., KONG, X.-Z., ZITHA, P.L.J., SAAR, M.O., BRUHN, D.F., KNORNSCHILD, N., ALLAZ, J.M., ARCHER, C. & BREHME, M. 2025 Mixing-induced mineral precipitation in porous media: front development and its impact on flow and transport. *Water Resour. Res.* **61** (10), e2024WR039316.
KREFT, A. & ZUBER, A. 1978 On the physical meaning of the dispersion equation and its solutions for different initial and boundary conditions. *Chem. Engng Sci.* **33** (11), 1471–1480.
LE BORGNE, T., DENTZ, M. & CARRERA, J. 2008 Lagrangian statistical model for transport in highly heterogeneous velocity fields. *Phys. Rev. Lett.* **101** (9), 090601.
LE BORGNE, T., DENTZ, M. & VILLERMAUX, E. 2013 Stretching, coalescence, and mixing in porous media. *Phys. Rev. Lett.* **110** (20), 204501.
LESTER, D.R., DENTZ, M., BANDOPADHYAY, A. & LE BORGNE, T. 2021 The Lagrangian kinematics of three-dimensional Darcy flow. *J. Fluid Mech.* **918**, A27.
LESTER, D.R., DENTZ, M., BANDOPADHYAY, A. & LE BORGNE, T. 2022 Fluid deformation in isotropic darcy flow. *J. Fluid Mech.* **945**, A18.
LESTER, D.R., DENTZ, M. & LE BORGNE, T. 2016 Chaotic mixing in three-dimensional porous media. *J. Fluid Mech.* **803**, 144–174.
LESTER, D.R., DENTZ, M., LE BORGNE, T. & DE BARROS, F.P.J. 2018 Fluid deformation in random steady three-dimensional flow. *J. Fluid Mech.* **855**, 770–803.
LESTER, D.R., DENTZ, M., SINGH, P. & BANDOPADHYAY, A. 2023 Under what conditions does transverse macrodispersion exist in groundwater flow? *Water Resour. Res.* **59** (3), e2022WR033059.
LESTER, D.R., HEYMAN, J., MÉHEUST, Y. & LE BORGNE, T. 2025 A unified theory of pore-scale chaotic advection. *J. Fluid Mech.* **1017**, A13.
LESTER, D.R., METCALFE, G. & TREFRY, M.G. 2013 Is chaotic advection inherent to porous media flow? *Phys. Rev. Lett.* **111** (17), 174101.
LEVY, M. & BERKOWITZ, B. 2003 Measurement and analysis of non-Fickian dispersion in heterogeneous porous media. *J. Contam. Hydrol.* **64** (3–4), 203–226.
LE BORGNE, T., DENTZ, M. & VILLERMAUX, E. 2015 The lamellar description of mixing in porous media. *J. Fluid Mech.* **770**, 458–498.
METCALFE, G., LESTER, D. & TREFRY, M. 2023 A primer on the dynamical systems approach to transport in porous media. *Transport Porous Med.* **146** (1), 55–84.
MOFFATT, H.K. 1969 The degree of knottedness of tangled vortex lines. *J. Fluid Mech.* **35** (1), 117–129.
MORALES, V.L., DENTZ, M., WILLMANN, M. & HOLZNER, M. 2017 Stochastic dynamics of intermittent pore-scale particle motion in three-dimensional porous media: experiments and theory. *Geophys. Res. Lett.* **44** (18), 9361–9371.
NEUMAN, S.P. & TARTAKOVSKY, D.M. 2009 Perspective on theories of non-Fickian transport in heterogeneous media. *Adv. Water Resour.* **32** (5), 670–680.
NOETINGER, B., ROUBINET, D., RUSSIAN, A., LE BORGNE, T., DELAY, F., DENTZ, M., DE DREUZY, J.-R. & GOUZE, P. 2016 Random walk methods for modeling hydrodynamic transport in porous and fractured media from pore to reservoir scale. *Transport Porous Med.* **115** (2), 345–385.
PAINTER, S. 1996 Evidence for non-Gaussian scaling behavior in heterogeneous sedimentary formations. *Water Resour. Res.* **32** (5), 1183–1195.
POLLOCK, D.W. 1988 Semianalytical computation of path lines for finite-difference models. *Groundwater* **26** (6), 743–750.
PUYGUIRAUD, A., GOUZE, P. & DENTZ, M. 2019 Upscaling of anomalous pore-scale dispersion. *Transport Porous Med.* **128** (2), 837–855.
REBENSHTOK, A., DENISOV, S., HÄNGGI, P. & BARKAI, E. 2014 Infinite densities for Lévy walks. *Phys. Rev. E* **90**, 062135.
ROLLE, M. & LE BORGNE, T. 2019 Mixing and reactive fronts in the subsurface. *Rev. Mineral. Geochem.* **85** (1), 111–142.
RUAN, F. & MCLAUGHLIN, D. 1998 An efficient multivariate random field generator using the fast fourier transform. *Adv. Water Resour.* **21** (5), 385–399.
RUBIN, Y. 2003 *Applied Stochastic Hydrogeology*. Oxford University Press.

https://doi.org/10.1017/jfm.2026.12192 Published online by Cambridge University Press

SOUZY, M., LHUISSIER, H., MÉHEUST, Y., LE BORGNE, T. & METZGER, B. 2020 Velocity distributions, dispersion and stretching in three-dimensional porous media. *J. Fluid Mech.* **891**, A16.

SPOSITO, G. 1994 Steady groundwater flow as a dynamical system. *Water Resour. Res.* **30** (8), 2395–2401.

TABOR, M. 1992 Stretching and alignment in general flow fields: classical trajectories from Reynolds number zero to infinity. In *Topological Aspects of the Dynamics of Fluids and Plasmas* (ed. H.K. Moffatt, G.M. Zaslavsky, P. Comte & M. Tabor), pp. 83–110. Springer.

VILLERMAUX, E. 2019 Mixing versus stirring. *Annu. Rev. Fluid Mech.* **51** (1), 245–273.

ZABURDAEV, V., DENISOV, S. & KLAFTER, J. 2015 Lévy walks. *Rev. Mod. Phys.* **87**, 483–530.

https://doi.org/10.1017/jfm.2026.12192 Published online by Cambridge University Press